DNS of a Plane Mixing Layer for the Investigation of Sound Generation Mechanisms

Andreas Babucke [a] Markus Kloker [a] Ulrich Rist [a]

[a]*Institut für Aerodynamik und Gasdynamik, Universität Stuttgart, Pfaffenwaldring 21, D-70550 Stuttgart, Germany*

Abstract

Direct numerical simulations in two and three dimensions have been performed to investigate the sound generation by vortex pairing in a compressible plane mixing layer with $Ma_1 = 0.5$ being the upper and $Ma_2 = 0.25$ being the lower stream Mach number. The Reynolds number based on the vorticity thickness at the inflow and the velocity of the upper stream is $Re = 500$. The flow is forced at the inflow with eigenfunctions obtained from viscous linear stability theory including three-dimensional disturbances. The results are verified with linear stability theory and the two-dimensional simulations performed by Colonius, Lele and Moin [6]. The excitation of a steady longitudinal vortex mode leads to an early three-dimensional deformation of the travelling spanwise vortices and reduced sound emission to the slower fluid stream side.

Key words: direct numerical simulation, mixing layer, sound generation
PACS: 43.28.-g, 47.15.St, 47.20.Ft, 47.27.ek

1 Introduction

Noise reduction is an important issue for a wide range of applications like aircrafts and turbomachinery for example. Being part of the French-German DFG-CNRS Research Group "Noise Generation in Turbulent Flows", our motivation is to simulate both the compressible mixing layer itself as well as parts of the surrounding acoustic field. The term mixing layer describes a flow field composed of two streams with unequal velocities and serves as a model flow for the initial part of a jet. Even with the actual increased computational

Email address: babucke@iag.uni-stuttgart.de (Andreas Babucke).

power, resolved simulations of full jets are limited to relatively low Reynolds numbers [7] and the focus on the initial shear layer removes this limit. The subsonic mixing layer has been investigated previously with respect to sound generation. The acoustic radiation of instability waves in a supersonic mixing layer was discussed by Tam and Burton [14]. Bogey, Bailly and Juve [3] used a two-dimensional Large-Eddy-Simulation to simulate a hyperbolic-tangent velocity profile. Direct Numerical Simulations of a two-dimensional mixing layer have been performed by Colonius, Lele and Moin [6]. Bogey et al. aswell as Colonius et al. compared the acoustic far field with Lighthill's acoustic analogy [12] showing good agreement between simulations and the acoustic analogy.

Aeroacoustic computations face the problems of i) the large extent of the acoustic field compared to the flow field and ii) the low amplitudes of the emitted sound relative to pressure fluctuations of the instability waves inside the shear region. To minimize spurious numerical sound, the unsteady compressible Navier-Stokes equations are solved using high-order accurate spatial direct numerical simulations (DNS) with appropriate boundary conditions.

Verification of our DNS code is done by comparing the results with viscous linear stability theory and with the two-dimensional simulations performed by Colonius et al. [6], serving as a benchmark problem for the project. By additionally forcing the flow with spanwise periodic perturbations, the investigation of sound generation mechanisms is expanded to three-dimensional effects.

2 Computational Configuration

2.1 Numerical Scheme

For this problem we apply our newly designed DNS code which solves the three-dimensional unsteady compressible Navier-Stokes equations. In what follows, velocities are normalized by the inflow velocity $\overline{U}_\infty$ and all other quantities by their inflow values, marked with the subscript $_\infty$. Length scales are made dimensionless with a reference length $\overline{L}$ and the time t with $\overline{L}/\overline{U}_\infty$, where the overbar denotes dimensional values. Temperature dependence of viscosity μ is modelled using the Sutherland law:

$$\overline{\mu}(T) = \overline{\mu}(\overline{T}_\infty) \cdot T^{3/2} \cdot \frac{1 + T_s}{T + T_s} \ , \tag{1}$$

where $T_s = 110.4K/\overline{T}_\infty$ and $\overline{\mu}(\overline{T}_\infty = 280K) = 1.735 \cdot 10^{-5} kg/(ms)$. As a weak temperature dependence can be assumed, the Prandtl number $Pr = 0.71$ and

the ratio of specific heats $\kappa = 1.4$ are taken constant for air. We use the conservative formulation solving for density ρ, momentum densities in the three dimensions ρu, ρv, ρw and total energy per volume E.

The spatial discretization in streamwise (x) and normal (y) direction is done by 6th order compact finite differences. The tridiagonal equation systems of the compact finite differences are solved using the Thomas algorithm. To reduce the aliasing error, alternating up- and downwind-biased finite differences are used for convective terms as proposed by Kloker [10]. The second derivatives are evaluated directly which better resolves the second derivatives compared to applying the first derivative twice. The square of the modified wavenumber k^*_{mod} over k^* is shown for different schemes in figure 1. The exact solution for the second derivative is k^{*2}. While the relative error of the second derivatives is less than 1% up to a modified wavenumber of $k^* = 1.00$ or $k^* = 1.74$ for 4th and 6th order, respectively, the result of computing the first derivative twice is only good up to $k^* = 0.62$ and $k^* = 1.42$ accordingly. Due to that, our scheme provides a resolution advantage of factor 3 for the viscous terms compared to a standard scheme of 4th order, often used for compressible flows. Moreover, another advantage of direct second derivatives computation is the fact, that k^{*2}_{mod} does not vanish for the least resolved waves with $k^* = \pi$ providing better accuracy and stability of the code.
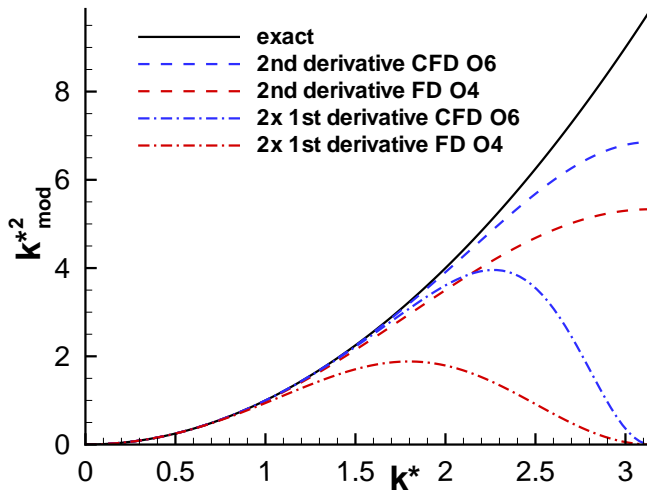

Fig. 1. Comparison of second derivative versus twice the first derivative for a wave with wave number $k^* = k \cdot \Delta x$.

Since the flow is assumed to be periodic in spanwise direction, we apply a spectral ansatz for the $z-$direction:

$$f(x, y, z, t) = \sum_{k=-K}^{K} \hat{F}_k(x, y, t) \cdot e^{i(k\gamma z)} . \tag{2}$$

3

f denotes any flow variable, $\hat{F}_k$ its complex Fourier coefficient, K the number of spanwise modes and $i = \sqrt{-1}$. The fundamental spanwise wavenumber γ is given by the fundamental wavelength λ_z representing the width of the integration domain by $\gamma = \frac{2\pi}{\lambda_z}$.

Spanwise derivatives are computed by transforming the respective variable into Fourier space, multiplying its spectral components with their wavenumbers $(i \cdot k \cdot \gamma)$ or square of their wavenumbers for the second derivatives and transforming them back into physical space. Due to the non-linear terms in the Navier-Stokes equations, higher harmonic spectral modes are generated at each timestep. To suppress aliasing, only 2/3 of the maximum number of modes for a specific z-resolution are used [4]. If a two-dimensional baseflow is used and disturbances of u, v, ρ, T, p are symmetric and disturbances of w are antisymmetric, flow variables are symmetric/antisymmetric with respect to $z = 0$. Therefore only half the number of points in spanwise direction are needed ($0 \leq z \leq \lambda_z/2$) and equation (2) is transferred to

$$f(x,y,z,t) = F_{0r}(x,y,z,t) + 2 \cdot \sum_{k=1}^{K} F_{kr}(x,y,t) \cdot \cos(k\gamma z) \tag{3}$$
$$\text{for } f \in [u, v, \rho, T, p]$$

$$f(x,y,z,t) = -2 \cdot \sum_{k=1}^{K} F_{ki}(x,y,t) \cdot \sin(k\gamma z) \tag{4}$$
$$\text{for } f \in [w] \, .$$

Arbitrary grid transformation in the x-y plane is provided by mapping the physical grid on an equidistant computational ξ-η grid:

$$x = x(\xi, \eta) \, , \; y = y(\xi, \eta) \, . \tag{5}$$

According to [1], the first derivatives can be computed as:

$$\frac{\partial}{\partial x} = \frac{1}{J} \left[\left(\frac{\partial}{\partial \xi} \right) \left(\frac{\partial y}{\partial \eta} \right) - \left(\frac{\partial}{\partial \eta} \right) \left(\frac{\partial y}{\partial \xi} \right) \right] \tag{6}$$

$$\frac{\partial}{\partial y} = \frac{1}{J} \left[\left(\frac{\partial}{\partial \eta} \right) \left(\frac{\partial x}{\partial \xi} \right) - \left(\frac{\partial}{\partial \xi} \right) \left(\frac{\partial x}{\partial \eta} \right) \right] \tag{7}$$

$$J = \begin{vmatrix} \frac{\partial x}{\partial \xi} & \frac{\partial y}{\partial \xi} \\ \frac{\partial x}{\partial \eta} & \frac{\partial y}{\partial \eta} \end{vmatrix} = \frac{\partial x}{\partial \xi} \cdot \frac{\partial y}{\partial \eta} - \frac{\partial y}{\partial \xi} \cdot \frac{\partial x}{\partial \eta} \tag{8}$$

with the metric coefficients $(\partial x/\partial \xi)$, $(\partial y/\partial \xi)$, $(\partial x/\partial \eta)$, $(\partial y/\partial \eta)$ and J being the determinant of the Jacobi matrix. To compute second spatial derivatives,

equations (6) and (7) are applied twice. Here one has to take into account that the metric coefficients and by that also the Jacobi determinant are a function of ξ and η as well.

Time integration is done using the standard 4th-order Runge-Kutta scheme as it is described in [10]. A hybrid parallelization based on domain decomposition in the x-y plane with internodal communication and shared-memory parallelization in spanwise direction allows to effectively use modern super vector computers like the NEC SX-8 installed at HLRS in Stuttgart. Details on the parallelization concept can be found in [2].

Non-reflective boundary conditions as described by Giles [8] are implemented at the inflow and the freestream boundaries. The inflow additionally allows to introduce defined disturbances with specific amplitudes and phases. To minimize reflections caused by oblique acoustic waves, a damping zone is applied at the upper and lower boundary, forcing the flow variables to a steady state solution. To avoid large structures passing the outflow, a combination of grid stretching and spatial low-pass filtering [11] is applied in the sponge region as done by Colonius, Lele and Moin [5]. Disturbances become increasingly badly resolved as they propagate through the sponge region and by applying a spatial filter, the perturbations are substantially dissipated before they reach the outflow boundary.

2.2 Flow parameters

For verification, the flow configuration has been closely matched to the case investigated by Colonius, Lele and Moin [6]. The Mach numbers of the upper and the lower stream are $Ma_1 = 0.5$ and $Ma_2 = 0.25$, respectively. As both stream temperatures are equal ($T_1 = T_2 = 280K$), the ratio of the streamwise velocities is $U_2/U_1 = 0.5$. The Reynolds number $Re = \rho_1 U_1 \delta / \mu = 500$ is based on the vorticity thickness at the inflow which is is used to normalize length scales:

$$\delta(x_0) = \left(\frac{\Delta U}{|\partial u / \partial y|_{max}} \right)_{x_0} . \tag{9}$$

The initial condition of the mixing layer is provided by solving the steady compressible two-dimensional boundary-layer equations. The initial coordinate $x_0 = 30$ is chosen such that the vorticity thickness at the inflow is 1. By that length scales are made dimensionless with δ. Velocities are normalized by U_1 and all other quantities by their values in the upper stream. Figure 2 shows the initial values at the inflow $x_0 = 30$.
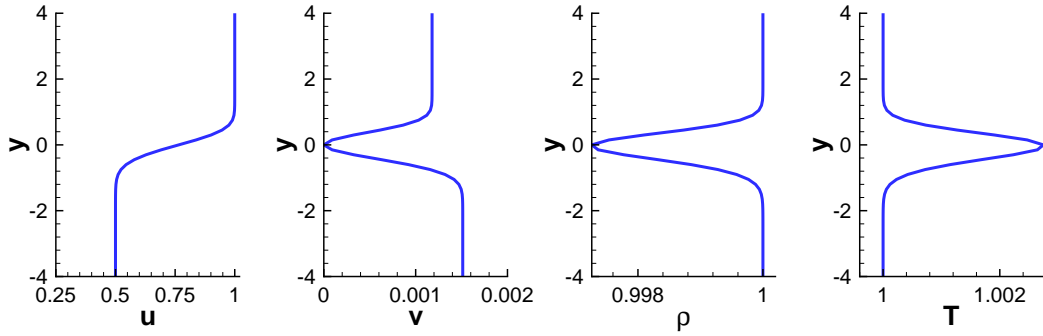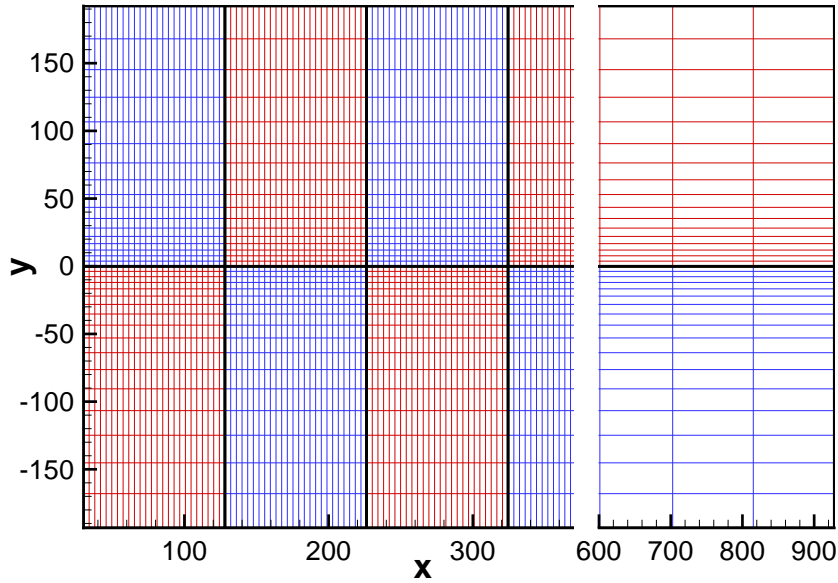
Fig. 2. Baseflow condition at the inflow $x_0 = 30$.

Fig. 3. Grid in x-y plane showing every 25th gridline and illustrating the domain decomposition and grid streching in the damping zone.

A cartesian grid of 2500 x 850 x 9 points in x-, y- and z-direction is used for $0 \leq z \leq \lambda_z/2$. In streamwise direction, the grid is uniform with spacing $\Delta x = 0.157$ up to the sponge region where the grid is highly stretched. In normal direction, the grid is continuously stretched with the smallest stepsize $\Delta y = 0.15$ in the middle of the mixing layer and the largest spacing $\Delta y = 1.06$ at the upper and lower boundaries. In both directions, smooth analytical functions are used to map the physical grid on the computational equidistant grid. In spanwise direction, the grid is uniform with a spacing of $\Delta z = 0.491$ which is equivalent to a spanwise wavenumber $\gamma_0 = 0.8$, where $\lambda_z/2 = \pi/\gamma_0 = 3.927$ is the spanwise extent of the domain. For parallelization, the total grid is decomposed into 8 domains as illustrated in figure 3.

3 Linear Stability Theory

To excite defined disturbances, the flow is forced at the inflow using eigen-functions from spatial viscous linear stability theory [13]. They have the form

$$\Phi = \hat{\Phi}_{(y)} \cdot e^{i(\alpha x + \gamma z - \omega t)} + c.c. \tag{10}$$

with $\Phi = (u', v', w', \rho', T', p')$ representing the set of disturbances of the primitive variables. The eigenfunctions are computed from the initial condition by combining a 4th order matrix-solver and Wielandt iteration. The y direction is resolved with 301 points and a stepsize of $\Delta y = 0.15$. The stability diagram in figure 4 shows the amplification rate at several x positions as a function of the frequency ω. The angular frequency is defined by $\omega = 2\pi \cdot \bar{f} \cdot \bar{\delta}(x_0)/\bar{U}_1$ with $\bar{f}$ in [Hz]. The fundamental frequency $\omega_0 = 0.6293$ was chosen in accordance with Colonius, Lele and Moin [6] having the largest amplification rate at the inflow $x_0 = 30$. Further downstream, the amplification rate decreases and its maximum moves towards lower frequencies. If α_i and ω are scaled with the streamwise growing local value of $\delta(x)$, the curves almost collapse like the low frequency band in figure 4. We note that we use viscous theory and not the Rayleigh equations like Colonius, Lele and Moin [6]. The growth rates and eigenfunctions thus differ up to 15% as can be seen from figures 4 and 6.
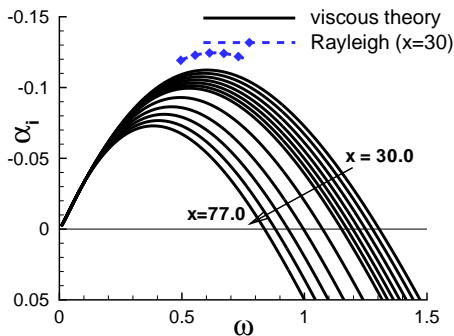

Fig. 4. Stability diagram for 2-d disturbances of the mixing layer at several x positions including inviscid theory (◇).
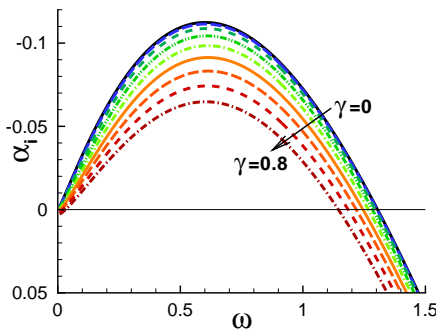
Fig. 5. Amplification rates in dependence of the spanwise wave number γ at the inflow $x_0 = 30$; $\Delta\gamma = 0.1$.

For oblique instability waves the amplifcation rates decrease while the maximum stays at the same frequency as illustrated in figure 5. The amplitude and phase distribution of an oblique wave with $\gamma = 0.8$, corresponding to a wave angle of approximately 45°, can be found in figure 7. The amplitude profile of the streamwise velocity u is narrower in the oblique case. The $v-$amplitude is shifted to the spanwise velocity w. For the thermodynamic parameters ρ, T and p, the maximum amplitudes are reduced by a factor of more than two compared to the two-dimensional case.
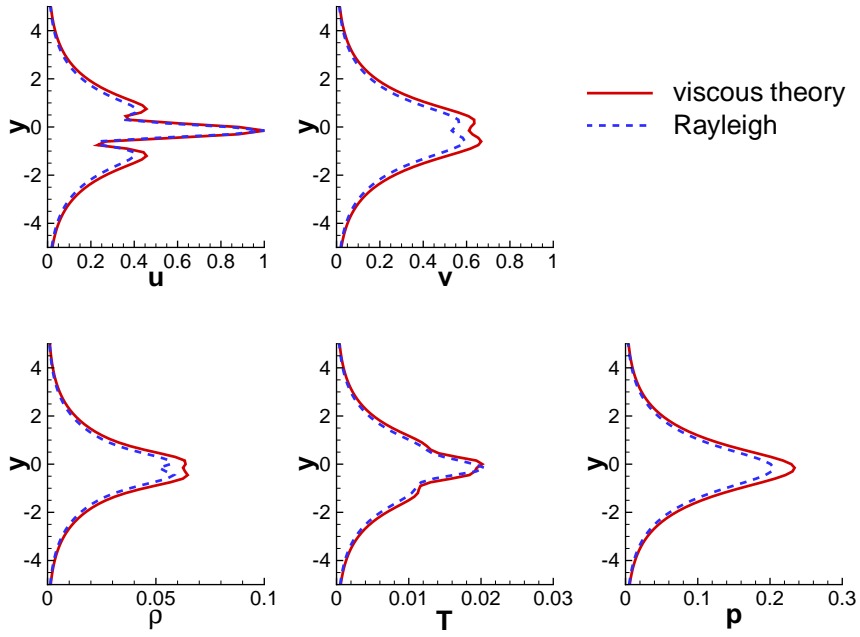
7

Fig. 6. Amplitudes of the eigenfunctions from spatial viscous theory compared with the results of the inviscid Rayleigh equations.
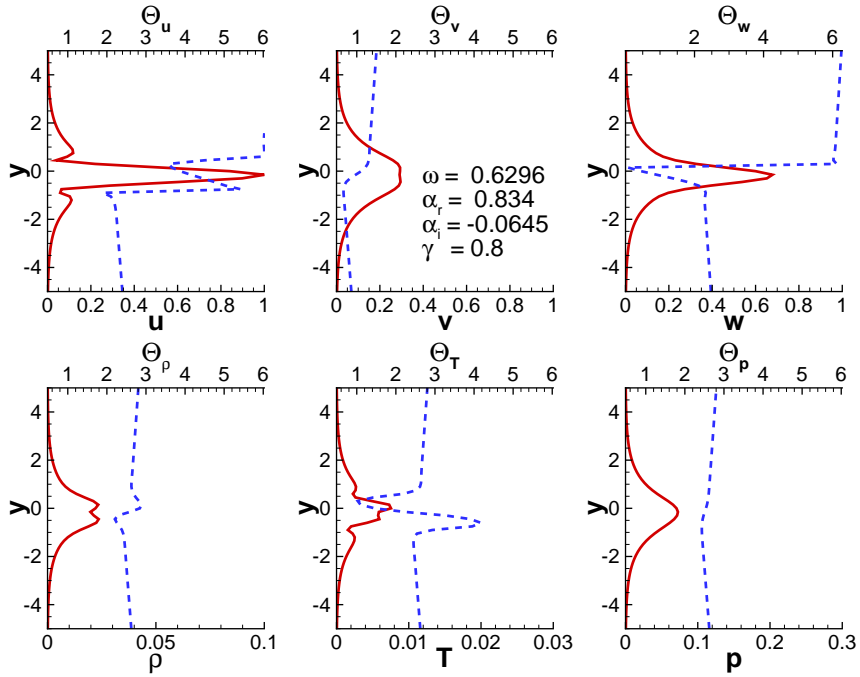

Fig. 7. Amplitude and phase (dashed) distribution of an instability wave with a spanwise wavenumber of $\gamma = 0.8$ at the inflow.

4 Results

Two different cases have been computed: in case A, the flow is forced only with two-dimensional eigenfunctions composed of the fundamental frequency $\omega_0 = 0.6293$ and the first three subharmonics similar to the computations of Colonius, Lele and Moin [6]. The amplitude of the fundamental frequency is 0.002 while the amplitudes of the subharmonics are 0.001. In accordance to the computations of Colonius, Lele and Moin [6], the phase shift is $\Delta\Theta = -0.028$ for the first, $\Delta\Theta = 0.141$ for the second subharmonic and $\Delta\Theta = 0.391$ radians for the third subharmonic disturbance. The amplitudes of the eigenfunctions are normalized by their maximum value of u and then scaled by the amplitude factor given above. As no three-dimensional disturbances are introduced, a two-dimensional simulation has been performed. Case B contains an additional one percent steady disturbance based on the eigenfunction of the three-dimensional unsteady mode with a spanwise wavenumber $\gamma = 0.8$ and the fundamental frequency ω_0. By using a relatively high amplitude compared to the unsteady disturbances, the two-dimensional waves can interact with the steady forcing and generate unsteady oblique waves.

In figures 8 and 9 the spanwise vorticity is shown after 68 periods of the fundamental frequency for the two- and three-dimensional cases, respectively. The initial region looks similar for both cases: the mixing layer rolls up into vortices with the fundamental mode being fully developed at a position of $x \approx 100$. The first pairing takes place in the area of $110 < x < 150$. The flowfield downstream of $x \approx 150$ differs for cases A and B. In the two-dimensional case the vortices develop further and a second vortex pairing is visible at $x \approx 200$, generating larger vortices passing with the second subharmonic frequency, showing good agreement with the reference case [6]. In the three-dimensional simulation, the vortices break up into small-scale structures as they approach the region of the second pairing. Further downstream, large scales almost disappear and the vorticity structures move in the negative $y-$direction compared with the two-dimensional case.

The λ_2 criterion [9] can be used to give a three-dimensional impression of the vortical structures. As shown in figure 10, the vortices are only slightly modulated in spanwise direction up to $x = 150$. Downstream of the position, where the vortices pair, the initially small three-dimensional structures form S-shaped longitudinal vortices which are twisted around their spanwise counterparts. Figure 11 shows an instantaneous view of the vorticity in $x-$direction together with the velocity field in an exemplary crossplane at $x = 161.2$ illustrating the S-shaped vortices. At $x \approx 200$ the spanwise vortices break up into small scale structures. While the flow field is dominated by small vortices further downstream, they are accumulated in groups generated with the wavelength of the second subharmonic mode.
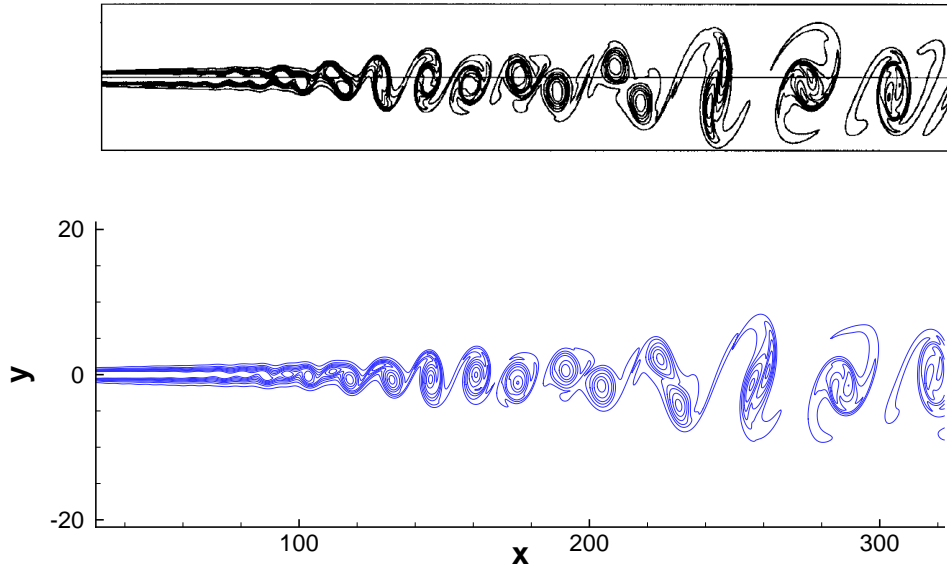
Fig. 8. Snapshot of the spanwise vorticity for computational case A with the y-axis being stretched by a factor of 2.5. Contour levels range from -0.26 to 0.02 with an increment of 0.04. The reference solution of Colonius, Lele and Moin [6] for the corresponding domain is shown above.
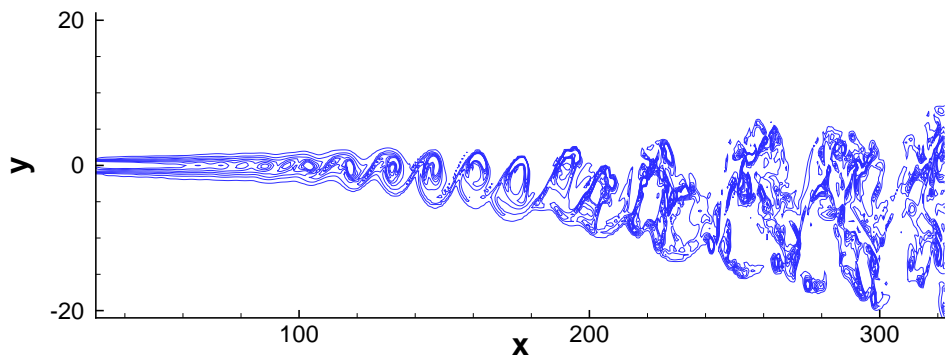

Fig. 9. Snapshot of the spanwise vorticity for computational case B at a spanwise position of $z = 0$ with contour levels as in figure 8.
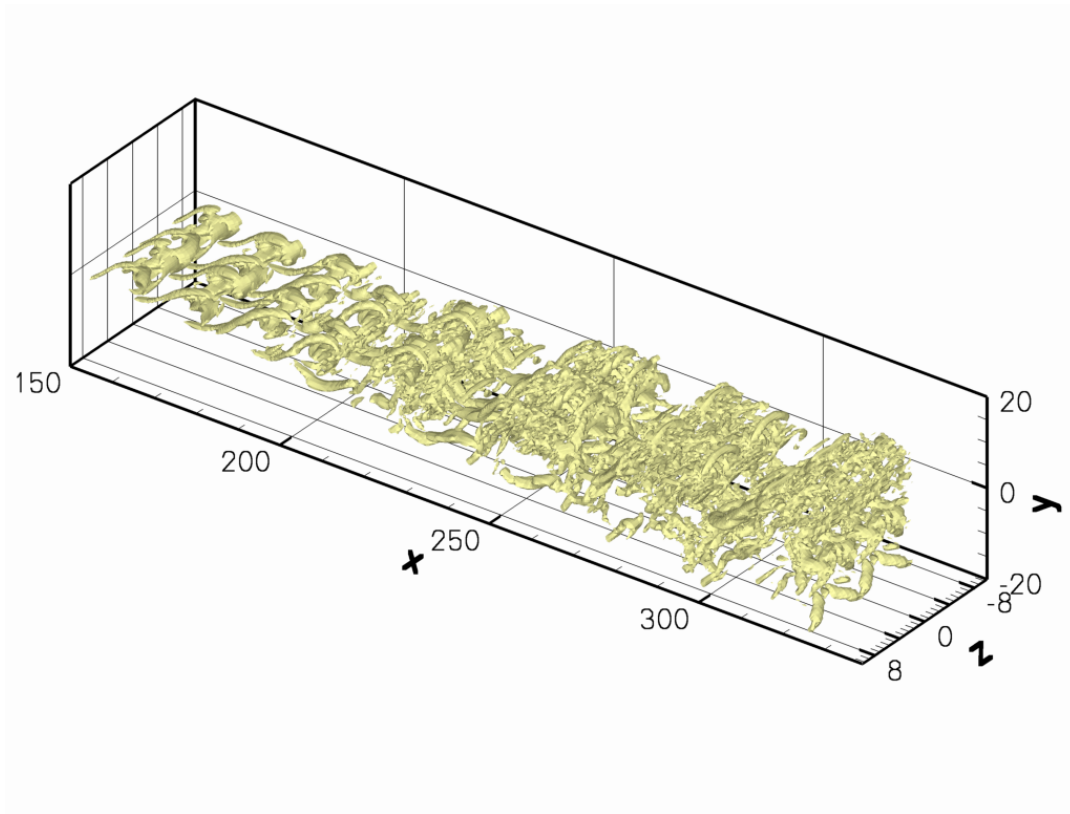
Fig. 10. Perspective view of the isosurface $\lambda_2 = -0.005$ in the range of two spanwise periods.
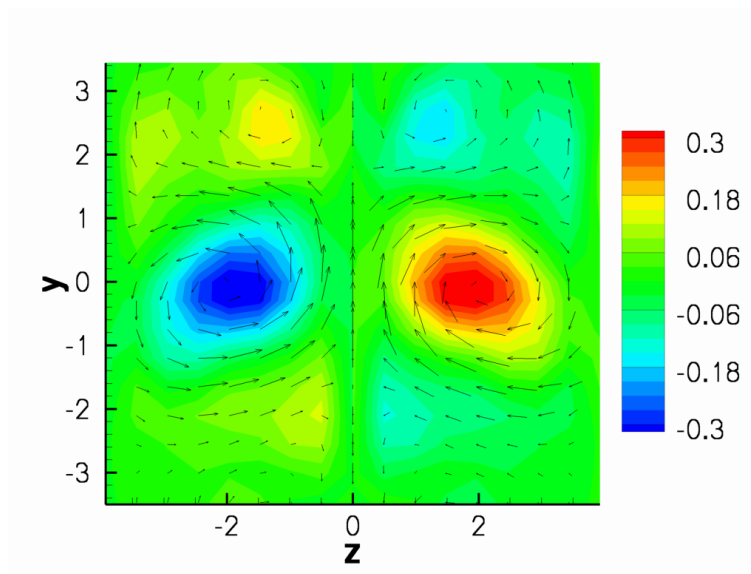
Fig. 11. Instantaneous view of the streamwise vorticity and the velocity field at a streamwise position of $x = 161.2$

The small difference in the spanwise vortices compared to the reference solution [6] is due to a slightly different forcing at the inflow. Of course, the spanwise resolution is not sufficient for the late stages. Highly resolved DNS will be performed for cases with parameters previously optimized using lower resolution DNS with case B being one of them.

For further analysis, a Fourier analysis in time and spanwise direction (for the three-dimensional case) is applied. The modes are denoted as (h, k) with h and k being the multiple of the fundamental frequency and the spanwise wavenumber, respectively. For both, amplitudes and amplification rates, the maximum amplitude along y is taken. The value considered for this analysis is the velocity component in $y-$direction v as its streamwise development is mainly associated to vorticity.

Figure 12 shows the amplitudes of the two-dimensional case. In the first part of the domain the amplitudes grow exponentially. The spatial growth rate α_i is compared with results from linear stability theory in figure 13. Although α_i is a very sensitive value, the mean values of the DNS correspond well to those predicted by linear stability theory. The agreement between simulation and theory serves as a verification of the computational scheme for small disturbances. Further downstream, the modes $(1, 0)$, $(1/2, 0)$ and $(1/4, 0)$ saturate at positions $x = 100$, $x = 150$ and $x = 250$, respectively, corresponding well to the positions where the respective vortices are fully developed (figure 8).

The amplitudes of the three-dimensional case are shown in figure 14. The excited steady mode $(0, 1)$ is slightly damped until $x = 110$ corresponding to the amplification rate given by linear stability theory (see figure 5). Downstream of $x = 110$ the non-linear generation of mode $(0, 1)$ exceeds the initial disturbance and saturation is observed. The unsteady two-dimensional modes $(1, 0)$, $(1/2, 0)$ and $(1/4, 0)$ grow exponentially up to $x \approx 70$ as in case A. A comparison of the growth rates is given in figure 15. The oblique waves $(1, 1)$, $(1/2, 1)$ and $(1/4, 1)$ are nonlinearly generated by the combination of two-dimensional waves with mode $(0, 1)$ as they are directly coupled with their corresponding two-dimensional modes. Therefore the amplitude growth does differ from linear behaviour where three-dimensional waves have a lower amplification than the two-dimensional waves.
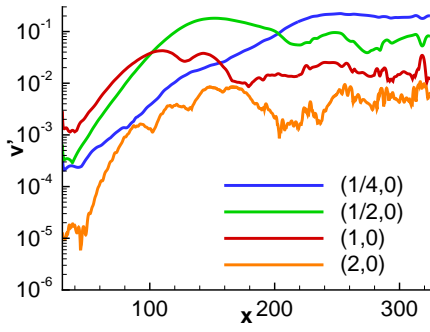
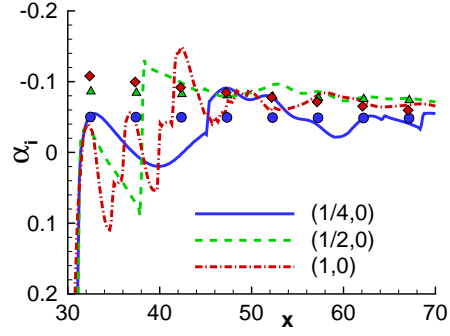Fig. 12. Maximum amplitudes of normal velocity v for the 2-d case A.

Fig. 13. Amplification rates of v based on max. amplitudes along y for case A (for symbols see Fig. 15).
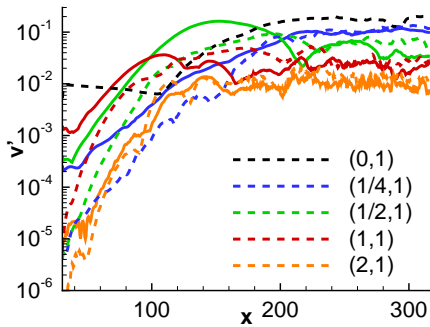

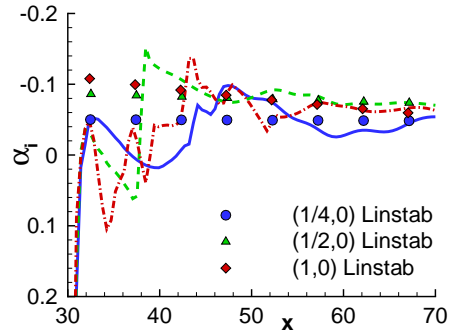Fig. 14. Maximum amplitudes of normal velocity v for the 3-d case B.

Fig. 15. Amplification rates of normal velocity v, based on maximum amplitudes along y for case B.

The resulting acoustic field can be visualized by plotting the dilatation, being $\nabla \cdot \vec{u}$, the divergence of the velocity field. The disturbance generation at the inflow itself produces acoustic waves, mainly at the fundamental and the first subharmonic frequency. A clearer picture of the acoustic field can be obtained by applying a Fourier transformation.

The Fourier transformed dilatation field is given in figures 16 for the two-dimensional and in figure 17 for the three-dimensional case for the second subharmonic.

In the two-dimensional case, the dominant accoustic source is located at $x \approx 240$, the position, where the vortices merge. The emitted sound is directed mainly downstream. Since the results closely match those given by Colonius, Lele and Moin [6], the computational scheme is thus verified for aeroacoustic simulations as well.
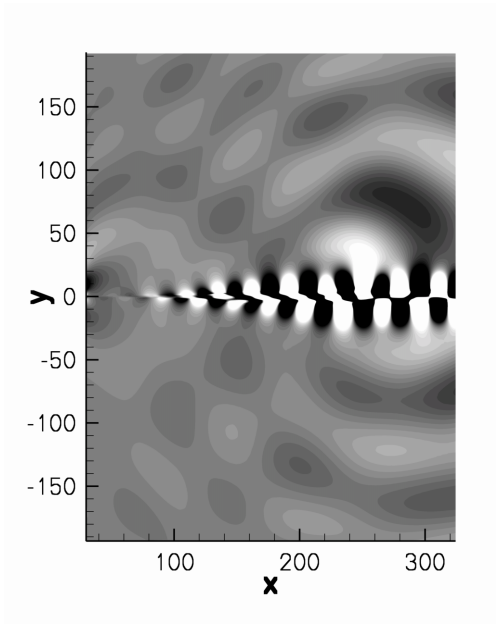
13

Fig. 16. Fourier transformed dilatation field of the second subharmonic for computational case A. Equidistant contour levels range from -10^{-5} to 10^{-5}.
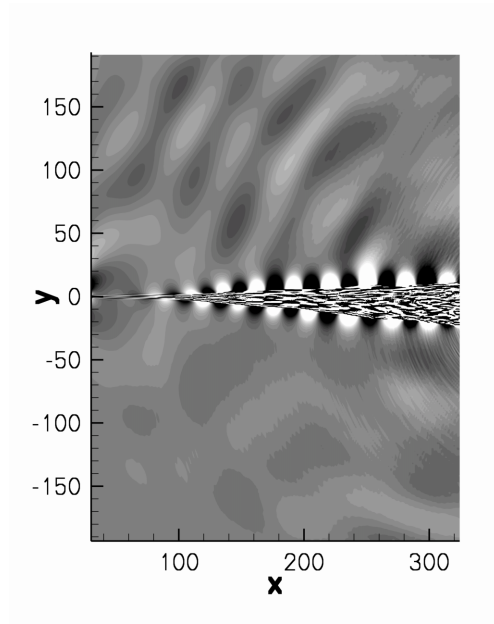

Fig. 17. Fourier transformed dilatation field of the second subharmonic for computational case B. Equidistant contour levels range from -10^{-5} to 10^{-5}.
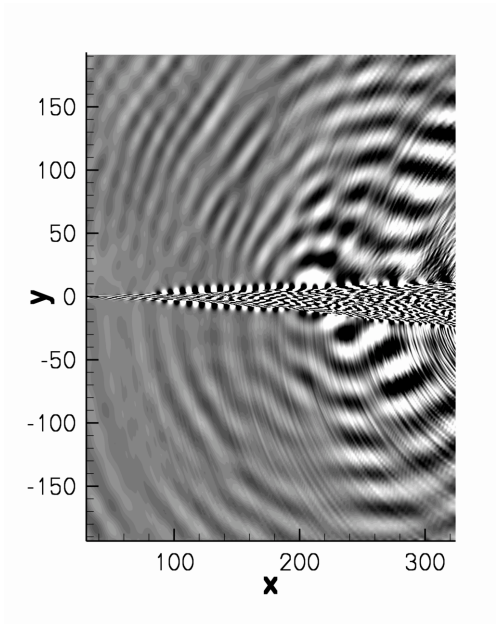

Fig. 18. Fourier transformed dilatation field of $3/4 \cdot \omega_0$ for computational case B. Equidistant contour levels range from -10^{-6} to 10^{-6}.
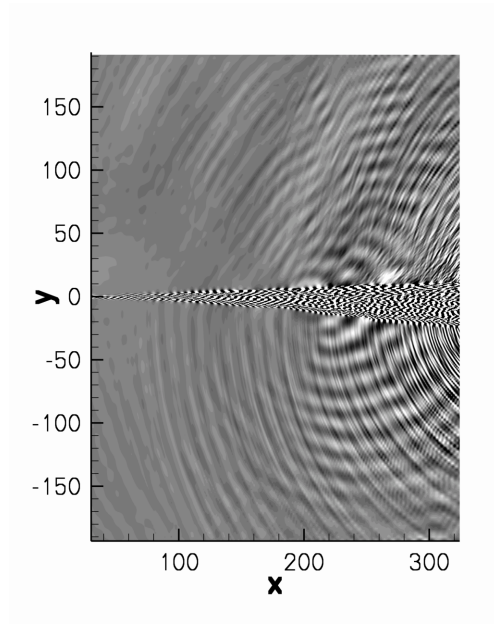

Fig. 19. Fourier transformed dilatation field of $5/4 \cdot \omega_0$ for computational case B. Equidistant contour levels range from -10^{-6} to 10^{-6}.

14

The different flowfield of case B leads to a different emitted sound. Figure 17 shows that the dominant noise source with the frequency $1/4 \cdot \omega_0$ of case A is missing. In figures 18 and 19 the Fourier-transformed dilatation field is given for frequencies $3/4 \cdot \omega_0$ and $5/4 \cdot \omega_0$, respectively. Here it can be seen that the tonal source from case A has transformed to broadband noise. Note that the contour levels in figures 18 and 19 are one magnitude smaller. The position of the noise source is located at $x = 210$, more upstream compared to the dominant acoustic source in case A.

The figures also show spurious waves emitted from the sponge region. As the wavelengths of these reflections are much smaller than the corresponding acoustic waves for these frequencies, they are in fact higher harmonics aliased to lower frequencies. A higher timewise sampling rate would be preferable, but the binary output already has a total file size of roughly 34GB.

5   Summary

A compressible isothermal mixing layer with the Mach numbers $Ma_1 = 0.5$ and $Ma_2 = 0.25$ for the upper and lower stream, respectively, has been simulated using two- and three-dimensional DNS. The results have been compared with linear stability theory and the two-dimensional simulation of Colonius, Lele and Moin [6] and very good agreement has been found. While the initial flow field of the three-dimensional computation with longitundinal-vortex-mode input is similar to the results of the two-dimensional simulation, small scale structures dominate the mixing layer further downstream. According to the differences in the flow itself, also the emitted sound differs: the sound generation in two dimensions is dominated by a tonal noise source, while in three dimensions, broad band noise is emitted. Investigations of the efficiency of passive control compared to active control based on the optimal control work of our French partners will be performed.

References

[1] J. D. Anderson. *Computational Fluid Dynamics*. McGraw-Hill, 1995.

[2] A. Babucke, J. Linn, M. Kloker, and U. Rist. Direct numerical simulation of shear flow phenomena on parallel vector computers. In *High performance computing on vector systems: Proceedings of the High Performance Computing Center Stuttgart 2005*. Springer Verlag Berlin, 2006.

[3] C. Bogey, C. Bailly, and D. Juve. Numerical simulation of sound generated by vortex pairing in a mixing layer. *AIAA J.*, 38(12):2210–2218, 2000.

[4] C. Canuto, M. Y. Hussaini, and A. Quarteroni. *Spectral methods in fluid dynamics*. Springer Series of Computational Physics. SpringerVerlag Berlin, 1988.

[5] T. Colonius, S. K. Lele, and P. Moin. Boundary conditions for direct computation of aerodynamic sound generation. *AIAA Journal*, 31(9):1574–1582, Sept. 1993.

[6] T. Colonius, S. K. Lele, and P. Moin. Sound generation in a mixing layer. *J. Fluid Mech.*, 330:375–409, 1997.

[7] J. B. Freund. Noise sources in a low-Reynolds-number turbulent jet at Mach 0.9. *J. Fluid Mech.*, 438:277–305, 2001.

[8] M. B. Giles. Nonreflecting boundary conditions for Euler equation calculations. *AIAA J.*, 28(12):2050–2058, 1990.

[9] J. Jeong and F. Hussain. On the identification of a vortex. *J. Fluid Mech.*, 285:69–94, 1995.

[10] M. J. Kloker. A robust high-resolution split-type compact FD scheme for spatial DNS of boundary-layer transition. *Appl. Sci. Res.*, 59:353–377, 1998.

[11] S. K. Lele. Compact finite difference schemes with spectral-like resolution. *J. Comp. Phys.*, 103:16–42, 1992.

[12] M. J. Lighthill. On sound generated aerodynamically. I. general theory. *Royal Society of London Proceedings Series A*, 211:564–587, 1952.

[13] L. M. Mack. Boundary-layer linear stability theory. In *AGARD Spec. Course on Stability and Transition of Laminar Flow*, volume R-709, 1984.

[14] C. Tam and D. Burton. Sound generated by instability waves of supersonic flows. part 1. two-dimensional mixing layers. *J. Fluid Mech.*, 138:249–271, 1984.